J Geod (2017) 91:1351–1366
DOI 10.1007/s00190-017-1029-7

ORIGINAL ARTICLE

Ionospheric and receiver DCB-constrained multi-GNSS single-frequency PPP integrated with MEMS inertial measurements

Zhouzheng Gao[1,2,3,4] · Maorong Ge[4] · Wenbin Shen[2] · Hongping Zhang[3] · Xiaoji Niu[3]

Received: 11 October 2016 / Accepted: 14 April 2017 / Published online: 18 May 2017

Abstract Single-frequency precise point positioning (SF-PPP) is a potential precise positioning technique due to the advantages of the high accuracy in positioning after convergence and the low cost in operation. However, there are still challenges limiting its applications at present, such as the long convergence time, the low reliability, and the poor satellite availability and continuity in kinematic applications. In recent years, the achievements in the dual-frequency PPP have confirmed that its performance can be significantly enhanced by employing the slant ionospheric delay and receiver differential code bias (DCB) constraint model, and the multi-constellation Global Navigation Satellite Systems (GNSS) data. Accordingly, we introduce the slant ionospheric delay and receiver DCB constraint model, and the multi-GNSS data in SF-PPP modular together. In order to further overcome the drawbacks of SF-PPP in terms of reliability, continuity, and accuracy in the signal easily blocking environments, the inertial measurements are also adopted in this paper. Finally, we form a new approach to tightly integrate the multi-GNSS single-frequency observations and inertial measurements together to ameliorate the performance of the ionospheric delay and receiver DCB-constrained SF-PPP. In such model, the inter-system bias between each two GNSS systems, the inter-frequency bias between each two GLONASS frequencies, the hardware errors of the inertial sensors, the slant ionospheric delays of each user-satellite pair, and the receiver DCB are estimated together with other parameters in a unique Kalman filter. To demonstrate its performance, the multi-GNSS and low-cost inertial data from a land-borne experiment are analyzed. The results indicate that visible positioning improvements in terms of accuracy, continuity, and reliability can be achieved in both open-sky and complex conditions while using the proposed model in this study compared to the conventional GPS SF-PPP.

✉ Wenbin Shen
wbshen@sgg.whu.edu.cn

Zhouzheng Gao
zhouzhenggao@whu.edu.cn

Maorong Ge
maor@gfz-potsdam.de

Hongping Zhang
hpzhang@whu.edu.cn

Xiaoji Niu
xjniu@whu.edu.cn

1 School of Land Science and Technology, China University of Geosciences, 29 Xueyuan Road, Beijing 100083, China

2 School of Geodesy and Geomatics, Wuhan University, 129 Luoyu Road, Wuhan 430079, China

3 GNSS Research Center, Wuhan University, 129 Luoyu Road, Wuhan 430079, China

4 German Research Centre for Geosciences (GFZ), Telegrafenberg, 14473 Potsdam, Germany

Keywords Single-frequency precise point positioning (SF-PPP) · Multi-constellation global navigations satellite systems (Multi-GNSS) · Inertial navigation system (INS) · Ionospheric delay and receiver DCB constraint (IC) · MEMS inertial measurements unit (IMU)

1 Introduction

Along with successive accuracy improvements on the satellites' precise orbit and clock products (Steigenberger et al. 2009; Kouba 2013) of global positioning system (GPS) and the rapid developments of multi-constellation global navigation satellite system (GNSS) (Montenbruck et al. 2014; Li et al. 2015), the performance of precise point positioning (PPP) (Héroux and Kouba 1995; Zumberge et al. 1997) has been ameliorated obviously, especially by applying the undifferenced ambiguities fixed model (Ge et al. 2008; Geng et al. 2010; Li et al. 2013), the slant ionospheric delay and receiver differential code bias (DCB) constraint model (Tu et al. 2013a, b; Zhang et al. 2013), and the PPP-RTK model (Geng et al. 2011; Teunissen and Khodabandeh 2015). Such achievements promoted the PPP based on dual-frequency GNSS observations being utilized widely in many engineering applications and scientific research domains, such as in the Earth surface deformation monitoring (Azúa et al. 2002; Larson et al. 2003; Xu et al. 2013), the meteorology research (Gendt et al. 2003; Li et al. 2015), the kinematic precise positioning (Gao and Shen 2002; Bock et al. 2003; Héroux et al. 2004), and the regional ionospheric modeling (Shi et al. 2012; Zhang et al. 2013).

Nevertheless, the GPS single-frequency PPP (SF-PPP) (Øvstedal 2002) has not been used as popular as the dual-frequency PPP (DF-PPP). Generally, it is mainly due to the fact that there exist no effective models that can be utilized to reduce the effect of the ionospheric delay in SF-PPP which may give rise to lower positioning accuracy and longer convergence time compared to the DF-PPP, especially in the kinematic applications. In order to overcome such drawback and upgrade the performance of SF-PPP, the Global Ionospheric Mapping (GIM) (Schaer et al. 1998) provided by International GNSS service (IGS) is recommended to be used to correct the ionospheric delay on pseudorange and carrier phase (Øvstedal 2002). Also, the single-frequency ionosphere-free combination (Montenbruck 2003) is an effective method that can be adopted in SF-PPP to eliminate the ionospheric delay on carrier phase, which is usually named as the Group and Phase Ionosphere Correction (GRAPHIC) model (Yunck 1996). However, because of the low accuracy of GIM (Hernández-Pajares et al. 2009) and the large noise of the single-frequency ionosphere-free combination (Gao et al. 2006), the SF-PPP positioning accuracy is still not sufficient. To solve this problem, Beran et al. (2003) proposed that the zenith ionospheric delay of each user-satellite pair can be estimated as parameters (Beran et al. 2003, 2004), which has been proved being able to obviously enhance the performance of SF-PPP (Gao et al. 2006). Besides, both the position accuracy and convergence time of the SF-PPP can also be ameliorated by using the precise global and regional ionospheric model (Le et al. 2009; Shi et al. 2012; Yao et al. 2013) and ambiguities resolution model (Odijk et al. 2012). Meanwhile, benefitting from the updated GLONASS and being established BDS and Galileo (Yang et al. 2011; Montenbruck et al. 2014), the performance of the SF-PPP can be upgraded visibly due to the significant enhancements of the satellites availability and continuity. Cai et al. (2013) evaluated the performance of the GPS + GLONASS SF-PPP based on the single-frequency ionosphere-free combination using both static data and kinematic observations, and about 30% position root-mean square (RMS) improvements were achieved compared to GPS only SF-PPP solutions. Lou et al. (2015) presented a general model for both the DF-PPP and the SF-PPP using the GPS + BDS + GLONASS + Galileo raw observations with the zenith ionospheric delay constraint, and their results calculated from multi-GNSS Experiment (MGEX) data demonstrated an improved performance of the general PPP models.

However, as a passive radio positioning mode, the final performance of the GNSS depends directly on the quality of the satellite signal tracking (Kleusberg and Teunissen 1996; Bisnath and Gao 2009). Hence, all of the positioning methods based on the GNSS observations may not work when partial or all of the GNSS signals are lost (Gao et al. 2015). Although the cycle-slip fixed algorithm (Zhang and Li 2012) can partially improve the performance of the PPP after the satellite signals are locked again, there are no output solutions during the GNSS outages periods. In order to obtain the positions during the GNSS outage situations, the integration system between the GPS and the inertial navigation system (INS) was proposed (Cox 1978), in which the advantages of both GPS and INS can be utilized and their drawbacks can be conquered effectively (Siouris 1993; Kim et al. 1998; Grejner-Brzezinska et al. 1998; Farrell and Barth 1999). In such system, the INS can provide users continuous and high rate navigation solutions during the GPS outage periods by only processing the velocity and angle data output from the Inertial Measurement Unit (IMU) sensor without any other external observations. Meanwhile, the errors of the IMU can be estimated and compensated online which can further improve the performance of the INS significantly (Shin and El-Sheimy 2003; Petovello 2004; Zhang and Gao 2005; Shin 2006). Recently, quite a few of studies have focused on the integration of the dual-frequency PPP and the INS using both single-GPS data (Roesler and Martell 2009; Du 2010; Rabbou and El-Rabbany 2015; Gao et al. 2015) and multi-GNSS data (Gao et al. 2016). The results show that the performance of PPP in terms of positioning accuracy and convergence speed can be improved obviously by the INS in both open-sky environments and challenged conditions.

Compared to the DF-PPP, the single-frequency PPP is much more cost effective. Thus, it is worth to do efforts to further improve the performance of the single-frequency PPP. In this paper, based on the previous studies on the SF-PPP, in order to further improve the positioning performance of the SF-PPP at present condition, we proposed the new algorithm of the single-frequency PPP, in which the slant ionospheric delay and receiver DCB constraint model, multi-GNSS data, and MEMS INS measurements will be integrated together. In this new SF-PPP mode, the positioning performance can be enhanced evidently by aiding relevant constraints and the INS augmentation, and the details about the methodology and the software implementation will be introduced in Sect. 2. Then, a land-borne experiment was arranged and GNSS outages were simulated to validate the performance of the augmented SF-PPP in kinematic applications as described in Sects. 3 and 4. Finally, key conclusions are provided in Sect. 5.

2 Kinematic single-frequency PPP augmentation model

In this section, the mathematical model of the augmented SF-PPP will be investigated. First, the raw observational functions of single-frequency GNSS will be given. Then, it is followed by the observational model of the slant ionospheric delay and receiver DCB constraint SF-PPP, the INS-augmented SF-PPP, the corresponding method of the parameter modeling and the adjustment, and the implementation of the whole system.

2.1 Single-frequency GNSS observational function model

Generally, the pseudo-range and carrier-phase observations on f_1 frequency (i.e. GPS L1: 1575.42 MHz; BDS B1: 1562.098 MHz; GLONASS L1: 1602.006 + k 0.5625 MHz, where k is the corresponding frequency coefficient) are adopted in the SF-PPP. The corresponding linearization observations for SF-PPP can be expressed as

$$P^s_{O,r,f_1} - P^s_{C,r,f_1} = \boldsymbol{u}^s_r \delta p_r + \delta t_r + m^s_w \delta T_{w,ztd} + \delta I^s_{r,f_1} + \delta d^s_{r,f_1} + \varepsilon_{P^s}, \varepsilon_{P^s} \sim N\left(0, \sigma^2_{P^s}\right) \quad (1)$$

$$L^s_{O,r,f_1} - L^s_{C,r,f_1} = \boldsymbol{u}^s_r \delta p_r + \delta t_r + m^s_w \delta T_{w,ztd} - \delta I^s_{r,f_1} - \lambda^s_{f_1} \delta N^s_{r,f_1} + \varepsilon_{L^s}, \varepsilon_{L^s} \sim N\left(0, \sigma^2_{L^s}\right) \quad (2)$$

where the symbols O and C refer to the observed and computed GNSS pseudo-range (P) and carrier phase (L) on f_1; the superscripts s and r denote the GNSS systems (s =GPS, BDS, and GLONASS) and receiver, respectively; $\mathbf{u}^s_r$ and m^s_w stand for the direction cosine matrix of each receiver–satellite pair and the global mapping function (GMF) of the wet component of the tropospheric delay (Böhm et al. 2006); δ represents error; p_r and t_r are the receiver position and the receiver clock offset; $T_{w,ztd}$ and I^s_{r,f_1} express the zenith total delay of the wet tropospheric delay and the slant ionospheric delay on f_1; d^s_{r,f_1} is the receiver DCB; $\lambda^s_{f_1}$ and N^s_{r,f_1} represent the carrier-phase wavelength and the float ambiguity; ε_{P^s} and ε_{L^s} are the sum of the observation noise and the unmodeled errors of the pseudo-range and carrier phase, respectively, with the corresponding apriori variance of $\sigma^2_{P^s} = 0.6$ m and $\sigma^2_{L^s} = 0.003$ m, and meanwhile the satellite-elevation-angle-depended model (Gendt et al. 2003) will also be applied to obtain the suitable apriori variance for the observations of different satellites.

2.2 Slant ionospheric delay and receiver DCB-constrained multi-GNSS SF-PPP observational functions

For the SF-PPP, the crux is to weaken the impact of the residual of the slant ionospheric delay in Eqs. (1) and (2), and the effect of the receiver DCB in Eq. (1) on the SF-PPP. In general, the previous researches on the SF-PPP are mainly focused on degrading the influence of the ionospheric delay (Øvstedal 2002; Montenbruck 2003; Beran et al. 2003, 2004). In the GIM correction model, the undisposed receiver DCB and the residual of the ionospheric delay may contaminate the performance of the SF-PPP (Øvstedal 2002). In the ionosphere-free combination (Yunck 1996; Montenbruck 2003), although the ionospheric delay on the carrier phase can be eliminated by taking the averaging between the pseudo-range and the carrier phase, such combination also makes the carrier-phase noise much larger. Besides, the receiver DCB is also absorbed by the float ambiguity in the IF SF-PPP which will destroy the constant character of the float ambiguity. The ionospheric delay effect on SF-PPP can be ignored by using the parameterization model without considering the receiver DCB (Beran et al. 2003, 2004). In order to overcome the drawbacks in these models, the slant ionopheric delays of each receiver–satellite pair and receiver DCB are parameterized and constrained by a priori model according to the studies of Tu et al. (2013a) and Zhang et al. (2013).

Based on previous studies on the dual-frequency GNSS ionopsheric and the receiver DCB constraint PPP (Tu et al. 2013a; Zhang et al. 2013; Li et al. 2013, 2015; Teunissen and Khodabandeh 2015), the linearization observations for the slant ionopsheric delays and the receiver DCB-constrained SF-PPP in the GPS + BDS + GLONASS case can be written as

$$\begin{bmatrix} \boldsymbol{P}^G_{O,r,f_1} \\ \boldsymbol{P}^B_{O,r,f_1} \\ \boldsymbol{P}^R_{O,r,f_k} \\ \boldsymbol{L}^G_{O,r,f_1} \\ \boldsymbol{L}^B_{O,r,f_1} \\ \boldsymbol{L}^R_{O,r,f_k} \end{bmatrix} - \begin{bmatrix} \boldsymbol{P}^G_{C,r,f_1} \\ \boldsymbol{P}^B_{C,r,f_1} \\ \boldsymbol{P}^R_{C,r,f_k} \\ \boldsymbol{L}^G_{C,r,f_1} \\ \boldsymbol{L}^B_{C,r,f_1} \\ \boldsymbol{L}^R_{C,r,f_k} \end{bmatrix} = \begin{bmatrix} \boldsymbol{u}^G_r \delta p_r + \delta t_r + m^G_w \delta T_{w,ztd} + \delta I^G_{r,f_1} + d^G_{r,f_1} \\ \boldsymbol{u}^B_r \delta p_r + \delta t_r + m^B_w \delta T_{w,ztd} + \delta I^B_{r,f_1} + d^B_{r,f_1} \\ \boldsymbol{u}^R_r \delta p_r + \delta t_r + m^R_w \delta T_{w,ztd} + \delta I^R_{r,f_k} + d^R_{r,f_k} \\ \boldsymbol{u}^G_r \delta p_r + \delta t_r + m^G_w \delta T_{w,ztd} - \delta I^G_{r,f_1} - \lambda^G_{f_1} \delta N^G_{r,f_1} \\ \boldsymbol{u}^B_r \delta p_r + \delta t_r + m^B_w \delta T_{w,ztd} - \delta I^B_{r,f_1} - \lambda^B_{f_1} \delta N^B_{r,f_1} \\ \boldsymbol{u}^R_r \delta p_r + \delta t_r + m^R_w \delta T_{w,ztd} - \delta I^R_{r,f_k} - \lambda^R_{f_k} \delta N^R_{r,f_k} \end{bmatrix} \quad (3)$$

where G, B, and R refer to GPS, BDS, and GLONASS respectively; the other parameters are the same as in (1) and (2).

To make sure the slant ionospheric delay can be estimated as precise as possible, a temporal and spatial correlation virtual observation function for each ionospheric delay is applied, which can be expressed as

$$I_{r,f_1}^s = 40.28 \cdot \mathrm{VTEC}/\left(f_1^2 \cos\left(Z_\theta\right)\right) + \varepsilon_{I_{r,f_1}^s},\ \varepsilon_{I_{r,f_1}^s} \sim N\left(0, \sigma^2_{\varepsilon_{I_{r,f_1}^s}}\right) \tag{4}$$

with the apriori variance (Zhang et al. 2013)

$$\sigma^2_{\varepsilon_{I_{r,f_1}^s}} = \begin{cases} \sigma_{I,0}^2/\sin^2(E), & t < 8 || 20 < t || B > \pi/3 \\ \left(\sigma_{I,0}^2 + \sigma_{I,1}^2 \cos(B)\cos\left(\frac{t-14}{12}\pi\right)\right)/\sin^2(E), & \text{other} \end{cases} \tag{5}$$

where VTEC and Z_θ refer to the vertical electronic content obtained from the GIM (Schaer et al. 1998) and the zenith angle at the ionosphere puncture point (IPP); $\varepsilon_{I_{r,f_1}^s}$ is the accuracy of the GIM model with the corresponding apriori variance $\sigma^2_{\varepsilon_{I_{r,f_1}^s}}$ as expressed in (5); E and B denote satellite elevation angle and the geodetic latitude of the receiver; t is the local time at IPP; $\sigma_{I,0}^2$ and $\sigma_{I,1}^2$ represent the variance of the zenith ionospheric delay and that of the zenith ionospheric delay variation with the apriori value of $\sigma_{I,0}^2 = \sigma_{I,1}^2 = 0.3$ m for the GIM model (Gao et al. 2015).

The dynamic model to describe the slant ionospheric delay variation can be defined as

$$I_{j,r,f_1}^s = I_{j-1,r,f_1}^s + \omega_{I_{j-1,r,f_1}^s},\ \omega_{I_{j-1,r,f_1}^s} \sim N\left(0, \sigma^2_{\omega_{I_{j-1,r,f_1}^s}}\right) \tag{6}$$

where $\sigma^2_{\omega_{I_{j,r,f_1}^s}}$ is the apriori variance of the ionospheric delay variation (ω_{I_{j,r,f_1}^s}); j denotes the epoch number. It should be noticed that the variation rate of the slant ionospheric delay is closely related to the satellite elevation angle. Hence, the satellite-elevation-angle-depended model (Gendt et al. 2003) is utilized to obtain the apriori variance of the slant ionospheric delay variation, and the expression can be written as

$$\sigma^2_{\omega_{I_{j-1,r,f_1}^s}} = \begin{cases} \sigma_{\omega_0}^2, & E \geq \pi/6 \\ \sigma_{\omega_0}^2/(2 \cdot \sin(E)), & E < \pi/6 \end{cases} \tag{7}$$

where $\sigma_{\omega_0}^2 = 0.03$ m/sqrt(h) is the basic apriori variance of the slant ionospheric delay variation (Gao et al. 2015).

Usually, there are hardware time delays in both transmitting terminal and receiving terminal. Such delays on carrier phase are called the uncalibrated phase delays (UPD) which are within ±0.5 cycle and can be absorbed by float ambiguity (Ge et al. 2008; Geng et al. 2010). Hence, it will not be considered in this SF-PPP. But, the hardware time delays on pseudo-range which cannot be absorbed, can be expressed in terms of the DCB, because the current satellites clock computation is based on the dual-frequency ionosphere-free combination, which can be defined as (Dach et al. 2007; Tu et al. 2013a)

$$\begin{bmatrix} d_{\mathrm{DCB}} \\ 0 \end{bmatrix} = \begin{bmatrix} 1 & -1 \\ \frac{f_1^2}{f_1^2-f_2^2} & -\frac{f_2^2}{f_1^2-f_2^2} \end{bmatrix} \begin{bmatrix} d_1 \\ d_2 \end{bmatrix} \tag{8}$$

where d_{DCB} stands for the DCB calculated by taking difference between the hardware time delays on pseudo-ranges P_1 and P_2. Whereas, the satellite DCB can be eliminated by using the DCB products from the IGS analysis center. The receiver DCB can be neither absorbed by parameters in the pseudo-range function (1) nor corrected by the existing products. To weaken the receiver DCB's impact on the performance of the PPP, it can be estimated as parameter as random walk procedure (Zhang et al. 2013). According to Eq. (8), the receiver hardware time delay on the pseudo-ranges P_1 can be further expressed as (Tu et al. 2013a; Li et al. 2015)

$$d_{r,f_1}^s = -f_2^2 \cdot d_{r,\mathrm{DCB}}/\left(f_1^2 - f_2^2\right) \tag{9}$$

with the corresponding random walk expression of

$$d_{j,r,f_1}^s = d_{j-1,r,f_1}^s + \omega_{d_{j-1,r,f_1}^s},\ \omega_{d_{j-1,r,f_1}^s} \sim N\left(0, \sigma^2_{\omega_{d_{j-1,r,f_1}^s}}\right) \tag{10}$$

where ω_{d_{j-1,r,f_1}^s} is the driving white noise of the receiver hardware time delay on P_1 with the apriori variance of $\sigma^2_{\omega_{d_{j-1,r,f_1}^s}} = 0.01$ m/sqrt(h) (Zhang et al. 2013). For the multi-GNSS case, due to different signal structures and frequencies adopted by each system, the receiver hardware time delays are not consonant with each other (Tu et al. 2013a; Li et al. 2015). Taking the receiver hardware time delay of the GPS as the basic value, the receiver hardware time delay between the BDS/GLONASS and the GPS are the inter-system biases (ISB). Besides, because the frequency-division multiple access (FDMA) technology is adopted by the GLONASS at present, the receiver hardware time delays of each GLONASS satellite are also a little different, and the difference between every two GLONASS frequencies is the inter-frequency bias (IFB). The estimates of the IFBs have been studied by many previous scholars, such as Tu et al. (2013a) and Li et al. (2015), etc. Generally, such DCBs can be estimated either as 1 basic DCB and 2 ISBs and $n_R - 1$

IFBs or as $2 + n_R$ independent DCBs (n_R is the available GLONASS numbers). In our study, we estimated the DCBs as independent parameters.

Finally, the observation functions of the slant ionospheric delay and the receiver DCB-constrained GPS + BDS + GLONASS SF-PPP will consist of 3^*n pseudo-range equations, 3^*n carrier-phase equations, n ionospheric related virtual equations and $2+n_R$ receiver DCB related virtual equations (n is the available numbers of GPS + BDS + GLONASS satellites). Then, the corresponding state vector will include the position, receiver clock, residual of the wet tropospheric zenith total delay, receiver DCB, inter-system biases, inter-frequency biases, slant ionospheric delays, and the float ambiguities for each satellite.

2.3 INS-augmented multi-GNSS SF-PPP linearization observational model

In the INS-augmented multi-GNSS SF-PPP model, the computed GNSS observations in Eq. (3) will be replaced by the INS predicted values (Gao et al. 2015, 2016). It was proved that the Doppler observations were conducive for estimating the INS sensor errors (Crespillo et al. 2014). Hence, after considering the virtual equations related to the slant ionospheric delay and receiver DCB, the corresponding observation equations for the INS-augmented multi-GNSS SF-PPP are written as

$$\begin{bmatrix} \boldsymbol{P}^s_{O,r,f_1} \\ \boldsymbol{L}^s_{O,r,f_1} \\ \boldsymbol{D}^s_{O,r,f_1} \\ \boldsymbol{I}^s_{r,f_1} \\ d^s_{r,f_1} \end{bmatrix} - \begin{bmatrix} \boldsymbol{P}^s_{\mathrm{INS},r,f_1} \\ \boldsymbol{L}^s_{\mathrm{INS},r,f_1} \\ \boldsymbol{D}^s_{\mathrm{INS},r,f_1} \\ \boldsymbol{I}^s_{\mathrm{INS},r,f_1} \\ d^s_{\mathrm{INS},r,f_1} \end{bmatrix} - \begin{bmatrix} l^s_p \\ l^s_p \\ l^s_v \\ 0 \\ 0 \end{bmatrix} = \begin{bmatrix} \boldsymbol{u}^s_r \delta p_r + \delta t_r + m^s_w \delta T_{w,ztd} + \delta \boldsymbol{I}^s_{r,f_1} + \delta d^s_{r,f_1} \\ \boldsymbol{u}^s_r \delta p_r + \delta t_r + m^s_w \delta T_{w,ztd} - \delta \boldsymbol{I}^s_{r,f_1} - \lambda^s_{f_1} \delta N^s_{r,f_1} \\ \boldsymbol{u}^s_r \delta v_r + \delta \dot{t}_r \\ \delta \boldsymbol{I}^s_{r,f_1} \\ \delta d^s_{r,f_1} \end{bmatrix} \tag{11}$$

where $_{\mathrm{INS}}$ denotes the INS predicted values; $\boldsymbol{D}$ represents the Doppler observations with the unit of m/s; l^s_p and l^s_v refer to the lever-arm corrections of position (p) and velocity (v) owning to the difference between the reference center of the GNSS receiver and the IMU sensor; the others symbols are the same as those in Eq. (3).

In order to predict the GNSS pseudo-range, carrier phase, and Doppler observations, the position and velocity of the satellites interpolated by precise orbit and clock products together with the position and velocity of the GNSS antenna updated by the INS mechanization using the increments of velocity and angle from the IMU (Shin 2006) are utilized. Generally, the mathematic model of the INS mechanization can be expressed as an integral process on the INS navigation differential equation, which can be written as

$$\begin{bmatrix} \boldsymbol{v}^n_{\mathrm{INS},t_k} \\ \boldsymbol{p}^n_{\mathrm{INS},t_k} \\ \boldsymbol{C}^n_{b,t_k} \end{bmatrix} = \int_{t_{k-1}}^{t_k} \begin{bmatrix} \boldsymbol{f}^n - \left(\boldsymbol{\omega}^n_{ie} + \boldsymbol{\omega}^n_{in}\right) \times \boldsymbol{v}^n_{\mathrm{INS}_{t_{k-1}}} + \mathbf{g}^n \\ \boldsymbol{v}^n_{\mathrm{INS}_{t_{k-1}}} \\ \left(\boldsymbol{\omega}^n_{ib} \times\right) - \left(\boldsymbol{\omega}^n_{in} \times\right) \boldsymbol{C}^n_{b,t_{k-1}} \end{bmatrix} dt \tag{12}$$

where $\boldsymbol{p}^n_{\mathrm{INS}}$, $\boldsymbol{v}^n_{\mathrm{INS}}$, and $\boldsymbol{C}^n_b$ denote the INS computed position, velocity, and attitude matrix for transform from body (b) frame (i.e., Forward-Right-Down) to navigation (n) frame (i.e., North-East-Down); $\boldsymbol{C}^n_b$ can be expressed in terms of Euler angle (roll, pitch, and heading); $\int_{t_{k-1}}^{t_k}()dt$ stands for the integral operation from epoch t_{k-1} to t_k; $\boldsymbol{f}^n$ and $\boldsymbol{\omega}^n_{ib}$ represent the specific force and the angular rate of the platform in navigation frame measured by accelerometer and gyroscope contained in IMU senor; $\boldsymbol{\omega}^n_{in}$ and $\boldsymbol{\omega}^n_{ie}$ are the rotation angular rate of n frame and Earth-centered Earth-fixed (e) frame (i.e., WGS84) with respect to inertial (i) frame projected in n-frame; $\mathbf{g}^n$ is the gravity.

Then, the INS-predicted values at the GNSS receiver antenna phase center can be expressed as

$$\begin{bmatrix} \boldsymbol{P}^s_{\mathrm{INS},r,f_1} + l^s_p \\ \boldsymbol{L}^s_{\mathrm{INS},r,f_1} + l^s_p \\ \boldsymbol{D}^s_{\mathrm{INS},r,f_1} + l^s_v \end{bmatrix} = \begin{bmatrix} \left\| p^s - \left(p^e_{\mathrm{INS}} + \boldsymbol{C}^e_n \boldsymbol{C}^n_b \boldsymbol{\iota}^b_{I-G}\right) \right\| + \Delta P^s_{f_1} \\ \left\| p^s - \left(p^e_{\mathrm{INS}} + \boldsymbol{C}^e_n \boldsymbol{C}^n_b \boldsymbol{\iota}^b_{I-G}\right) \right\| - \lambda^s_{f_1} N^s_{r,f_1} + \Delta L^s_{f_1} \\ \left\| v^s - v^e_{\mathrm{INS}} - \boldsymbol{C}^e_n \left(\left(\boldsymbol{\omega}^n_{in} \times\right) \boldsymbol{C}^n_b \boldsymbol{\iota}^b_{I-G} \right.\right. \\ \left.\left. + \boldsymbol{C}^n_b \left(\boldsymbol{\iota}^b_{I-G} \times\right) \boldsymbol{\omega}^b_{ib} \right) \right\| + \Delta D^s_{f_1} \end{bmatrix} \tag{13}$$

where p^s and v^s refer to the position and velocity of satellite in e-frame computed by precise satellite orbit and clock products; p^e_{INS} and v^e_{INS} denote the position at the IMU center in the geodetic coordinate system (latitude-longitude-height) and velocity at IMU center in e-frame which can be obtained from $\boldsymbol{p}^n_{\mathrm{INS}}$ and $\boldsymbol{v}^n_{\mathrm{INS}}$ in (12); $\boldsymbol{C}^e_n$ is used to transform from n-frame to e-frame; ι^b_{I-G} represents the lever-arm offset measured from the IMU center to the GNSS receiver antenna phase center in b-frame; $\Delta P^s_{f_1}$, $\Delta L^s_{f_1}$, and $\Delta D^s_{f_1}$ indicate the sum of the error corrections of the pseudo-range, carrier phase, and Doppler, respectively.

As mentioned above, the INS is usually operated in n-frame, and the position is expressed in terms of geodetic latitude (B), longitude (L), and height (h). Hence, according to Eq. (13), after considering $\delta \boldsymbol{C}^n_b = I - (\delta\theta \times)$ in small attitude variation ($\delta\theta$) condition and $\delta v^e_r = \delta\left(\boldsymbol{C}^e_n v^n_r\right) =$

$\boldsymbol{C}_n^e \delta v_r^n + \delta \boldsymbol{C}_n^e v_r^n$, the relationship between the increments of the position and velocity at the GNSS receiver antenna phase center in e-frame and these at the IMU measuring center in n-frame can be given by

$$\begin{bmatrix} \delta p_r \\ \delta v_r \end{bmatrix} = \begin{bmatrix} \boldsymbol{C}_1 \delta p_{\text{INS}}^n + \boldsymbol{C}_1 \left(\boldsymbol{C}_b^n \boldsymbol{\iota}_{I-G}^b \times \right) \delta\theta \\ \boldsymbol{C}_2 \delta p_{\text{INS}}^n + \boldsymbol{C}_n^e \delta v_{\text{INS}}^n - \boldsymbol{C}_n^e \gamma_1 \delta\theta \\ +\boldsymbol{C}_n^e \boldsymbol{C}_b^n \left(\iota_{I-G}^b \times \right) \delta\boldsymbol{\omega}_{ib}^b \end{bmatrix} \tag{14}$$

with

$$\boldsymbol{C}_1 = \begin{bmatrix} -\left(R_N + h\right)\sin(B)\cos(L)/\left(R_M + h\right) & -\sin(L) & -\cos(B)\cos(L) \\ -\left(R_N + h\right)\sin(B)\sin(L)/\left(R_M + h\right) & \cos(L) & -\cos(B)\sin(L) \\ \left(R_N\left(1 - e_0^2\right) + h\right)\cos(B)/\left(R_M + h\right) & 0 & \sin(B) \end{bmatrix} \tag{15}$$

$$\boldsymbol{C}_2 = \begin{bmatrix} -\cos(B)\cos(L)\boldsymbol{v}_N + \sin(B)\cos(L)\boldsymbol{v}_D & \sin(B)\sin(L)\boldsymbol{v}_N + \cos(B)\sin(L)\boldsymbol{v}_D & 0 \\ -\cos(B)\sin(L)\boldsymbol{v}_N + \sin(B)\sin(L)\boldsymbol{v}_D & -\sin(B)\cos(L)\boldsymbol{v}_N - \cos(B)\cos(L)\boldsymbol{v}_D & 0 \\ -\sin(B)\boldsymbol{v}_N - \cos(B)\boldsymbol{v}_D & 0 & \sin(B) \end{bmatrix} \tag{16}$$

$$\gamma_1 = \left(\omega_{in}^n \times\right) \boldsymbol{C}_b^n \left(\boldsymbol{\iota}_{I-G}^b \times\right) + \boldsymbol{C}_b^n \left(\boldsymbol{\iota}_{I-G}^b \times \omega_{ib}^b\right) \tag{17}$$

where $\boldsymbol{C}_1$ is used to transform the position increments from geodetic coordinate system to e-frame; $\boldsymbol{C}_2$ stands for the position-related coefficient derived from $\delta(\boldsymbol{C}_n^e v_r^n)$; γ_1 is the attitude related coefficient; v_E, v_N and v_D are the velocity at the GNSS receiver antenna center in n-frame; R_M, R_N, and e_0^2 represent the prime circle radius, the meridian radius, and the first eccentricity of the Earth ellipsoid; $\delta\omega_{ib}^b$ denotes the gyroscope errors with considering only the bias and the scale factor in this paper. Similarly, such kinds of errors also should be considered for accelerometers observations (Niu et al. 2006). In general, it can be written as

$$\begin{bmatrix} \delta\boldsymbol{\omega}_{ib}^b \\ \delta\boldsymbol{f}^b \end{bmatrix} = \begin{bmatrix} \boldsymbol{S}_g & 0 \\ 0 & \boldsymbol{S}_a \end{bmatrix} \begin{bmatrix} \boldsymbol{\omega}_{ib}^b \\ \boldsymbol{f}^b \end{bmatrix} + \Delta t \begin{bmatrix} \boldsymbol{B}_g \\ \boldsymbol{B}_a \end{bmatrix} \tag{18}$$

with the corresponding driving noise being modeled as 1st order Gauss–Markov process

$$\begin{bmatrix} \boldsymbol{S}_k \\ \boldsymbol{B}_k \end{bmatrix} = e^{-\Delta t/T} \begin{bmatrix} \boldsymbol{S}_{k-1} \\ \boldsymbol{B}_{k-1} \end{bmatrix} + \begin{bmatrix} \varsigma_{S_{k-1}} \\ \varsigma_{B_{k-1}} \end{bmatrix}, \begin{bmatrix} \varsigma_{S_{k-1}} \\ \varsigma_{B_{k-1}} \end{bmatrix} \sim N \begin{bmatrix} 0, 2\sigma_S^2 \Delta t/T \\ 0, 2\sigma_B^2 \Delta t/T \end{bmatrix} \tag{19}$$

where Δt and T indicate the interval of the IMU observations and the relative time of the IMU errors; σ_S^2 and σ_B^2 are the apriori variance of the scale factor ($\boldsymbol{S}$) and the bias ($\boldsymbol{B}$) which are mainly determined by the IMU sensor performance and can be obtained from the manufacturer or by calibration.

2.4 Parameters modeling and adjustment

According to the mathematical model of the Kalman filter (Brown and Hwang 1992), we have the observation function

$$\boldsymbol{Z}_j = \boldsymbol{H}_j \boldsymbol{X}_j + \varepsilon_j, \varepsilon_j \sim N(0, \boldsymbol{R}_j) \tag{20}$$

and the corresponding state function

$$\boldsymbol{X}_j = \boldsymbol{\Phi}_{j,j-1} \boldsymbol{X}_{j-1} + \xi_{j-1}, \xi_{j-1} \sim N(0, \boldsymbol{Q}_{j-1}) \tag{21}$$

where $\boldsymbol{Z}$, $\boldsymbol{H}$, and $\boldsymbol{R}$ denote, respectively, the innovation vector obtained from left side of Eq. (11), the design coefficient matrix derived from right side of Eq. (11), and the apriori variance of the measurements noise ($\boldsymbol{\varepsilon}$) based on Eqs. (5) and (7); $\boldsymbol{Q}$ and $\boldsymbol{\Phi}$ indicate the state noise ($\boldsymbol{\xi}$) variance of state vector ($\boldsymbol{X}$) and the corresponding transform matrix from j-1 epoch to j epoch according to the dynamic model of each state parameter, respectively. By introducing Eqs. (13) and (14) into Eq. (11), the state vector of the INS-augmented multi-GNSS SF-PPP can be obtained and expressed as

$$\boldsymbol{X} = \left[\delta p_{\text{INS}}^n \; \delta v_{\text{INS}}^n \; \delta\theta \; \boldsymbol{B}_{\text{IMU}} \; \boldsymbol{S}_{\text{IMU}} \; \delta\boldsymbol{t}_r \; \delta T_{w,ztd} \; \delta\boldsymbol{d}_{r,f_1}^s \; \delta\boldsymbol{N}_{r,f_1}^s \; \delta\boldsymbol{I}_{r,f_1}^s \right]^T \tag{22}$$

where $\boldsymbol{B}_{\text{IMU}} = \left[\boldsymbol{B}_g \; \boldsymbol{B}_a \right]$ and $\boldsymbol{S}_{\text{IMU}} = \left[\boldsymbol{S}_g \; \boldsymbol{S}_a \right]$ represent the biases and scale factors of gyroscopes and accelerometers; $\delta\boldsymbol{t}_r$ and $\delta\boldsymbol{d}_{r,f_1}^s$ refer to respectively the receiver clock error-related parameter (clock offset and drift) and receiver DCB error-related parameters; $\delta\boldsymbol{N}_{r,f_1}^s$ and $\delta\boldsymbol{I}_{r,f_1}^s$ denote the float ambiguities error and slant ionospheric delays error of each satellite.

It should be noticed that in the INS-augmented multi-GNSS SF-PPP, the PSI angle error model (Shin 2006) can be used to describe the dynamic behavior of position, velocity, and attitude, respectively, which can be defined as

$$\begin{bmatrix} \delta\boldsymbol{p}_{\text{INS},k}^n \\ \delta\boldsymbol{v}_{\text{INS},k}^n \\ \delta\theta_k \end{bmatrix} = \begin{bmatrix} \left(\boldsymbol{I} - \left(\boldsymbol{\omega}_{en}^n \times\right)\Delta t\right) \delta\boldsymbol{p}_{INS,k-1}^n + \delta\boldsymbol{v}_{\text{INS}}^n \Delta t \\ \left(\boldsymbol{I} - \left(\left(\boldsymbol{\omega}_{ie}^n + \boldsymbol{\omega}_{in}^n\right)\Delta t\right)\times\right) \delta\boldsymbol{v}_{\text{INS},k-1}^n \\ +\left(\boldsymbol{f}^n \times\right)\delta\theta_{k-1}\Delta t + \delta\mathbf{g}^n \Delta t + \boldsymbol{C}_b^p \delta\boldsymbol{f}^b \Delta t \\ -\boldsymbol{\omega}_{in}^n \times \delta\theta - \boldsymbol{C}_b^n \delta\boldsymbol{\omega}_{ib}^b \end{bmatrix} \tag{23}$$

Fig. 1 Implementation of the single-frequency PPP augmented by slant ionospheric delay and the receiver DCB constraint model, the multi-GNSS, and the inertial measurements

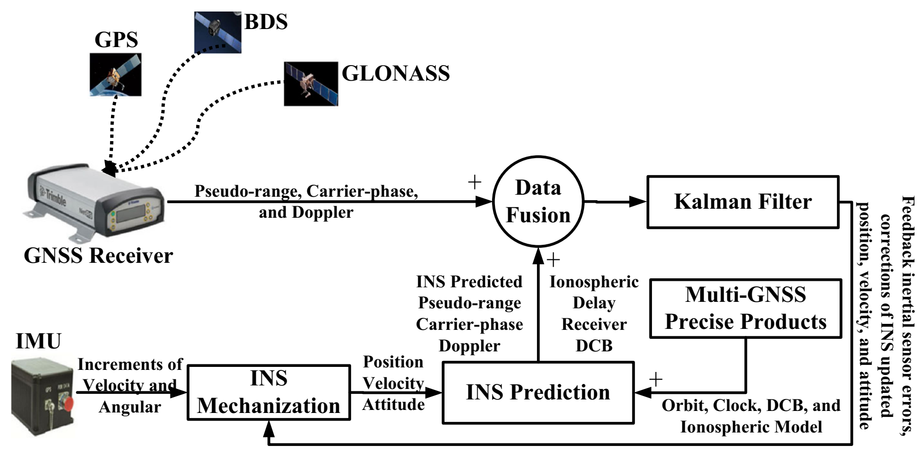

where, the symbols in Eq. (23) are the same as those in Eqs. (12), (15) and (18).

Meanwhile, the random constant model and the random walk procedure (Brown and Hwang 1992) are utilized to express the dynamic character of the float ambiguities and other parameter behaviors. Then, the $\boldsymbol{\Phi}$ can be obtained from these state models mentioned above, and the parameters in Eq. (22) can be estimated by using the Kalman filter (Brown and Hwang 1992)

$$\begin{bmatrix} \boldsymbol{X}_j \\ \boldsymbol{P}_j \end{bmatrix} = \begin{bmatrix} \boldsymbol{\Phi}_{j,j-1}\boldsymbol{X}_{j-1} + \boldsymbol{K}_j\left(\boldsymbol{Z}_j - \boldsymbol{H}_j\boldsymbol{\Phi}_{j,j-1}\boldsymbol{X}_{j-1}\right) \\ \left(\boldsymbol{I}-\boldsymbol{K}_j\right)\left(\boldsymbol{\Phi}_{j,j-1}\boldsymbol{P}_{j-1}\boldsymbol{\Phi}_{j,j-1}^T + \boldsymbol{Q}_{j-1}\right) \\ \left(\boldsymbol{I}-\boldsymbol{K}_j\right)^T + \boldsymbol{K}_j\boldsymbol{R}_j\boldsymbol{K}_j^T \end{bmatrix} \tag{24}$$

where $\boldsymbol{K}$ and $\boldsymbol{I}$ refer to the gain matrix and the unit matrix, respectively.

2.5 Implementation of augmented single-frequency PPP

According to the mathematic models introduced above, the SF-PPP augmented by the slant ionospheric delay and the receiver DCB constraint model, the multi-GNSS, and the INS can be implemented. As shown in Fig. 1, the increments of the velocity and angle collected by the IMU (accelerometer and gyroscope) will be processed in the INS mechanization phase to provide the navigation parameters (position, velocity, and attitude) in the n-frame at the IMU measuring center after the hardware errors (the biases and the scale factors) compensation. Then, these navigation parameters can be applied together with precise satellite orbits and clocks to predict the GNSS (GPS/BDS/GLONASS) observations. After that, the INS predicted pseudo-range, carrier phase, and Doppler observations at frequency f_1 are integrated with GNSS raw observations output from the GNSS receiver in Kalman filter. Finally, the enhanced SF-PPP solutions will be achieved and the inertial sensor errors will have a feedback operation to compensate the errors of the inertial data before processing the INS mechanization and correcting the INS navigation parameters.

3 Experiment and data processing methods

In order to evaluate the positioning performance of the new SF-PPP algorithm in kinematic applications, a group of the GPS + BDS + GLONASS single-frequency observations (collected by Trimble NetR9 multi-GNSS receiver) and a set of microelectromechanical sensor (MEMS) inertial measurements from a land-born vehicle test arranged around Wuhan in China during the local time from about 13.5 to 16.0 pm on 19 June, 2013, were processed and analyzed. During the test, the vehicle moved repeatedly along the northwest to the southeast direction with the maximum speed of ±25 m/s, and the trajectory was shown in Fig. 2. The rate of the GNSS data and the inertial measurements are 1 and 200 Hz,

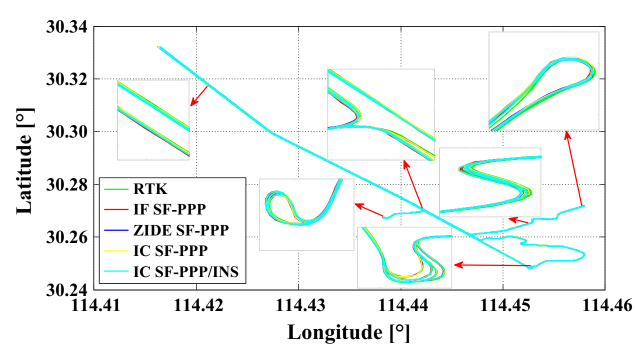

Fig. 2 Trajectories of the test calculated by different positioning models: RTK is the reference trajectory, IF SF-PPP, ZIDE SF-PPP, IC SF-PPP, and IC SF-PPP/INS denote the trajectories computed by single-frequency ionosphere-free combination PPP, zenith ionospheric delay estimation PPP, slant ionospheric delay and receiver hardware time delay constraint PPP, and INS augmentation and slant ionospheric delay and receiver hardware time delay constraint PPP, respectively; the sub-figures show the some details of the trajectory

respectively. The MEMS IMU (POS1100, manufactured by Wuhan MP Space Time Technology Company) consists of a triaxial MEMS gyroscope and a triaxial quartz accelerometer. According to the manufacturer information, the biases instability of the gyroscope and the accelerometer are $10^\circ/\mathrm{h}$ and $1.5\,\mathrm{cm/s^2}/h$, the corresponding scale factor instability is 1000 part per million (ppm), and the instabilities of the angle random walk (ARW) and the velocity random walk (VRW) are, respectively, 0.33°/sqrt(h) and 0.18 m/s/sqrt(h). The volume of POS1100 is $81.8 \times 68 \times 70$ mm, and its mass is less than 0.5 kg. Theoretically, POS1100 can work in the environment with the temperature from -45 to $+71$ °C, and the operating power is 4 W with the range of voltage direct current between 9 and 36 V.

3.1 Data processing schemes

For the single-frequency GNSS data processing, the satellite cutoff elevation angle is set to 7.5°. To eliminate and weaken the impacts of the satellite-related errors (i.e., satellite orbit and clock error, satellite DCB, satellite phase center offset and variation) on positioning accuracy, the precise satellite orbit and clock products for the GPS/BDS/GLONASS from Wuhan University and the products of the satellite DCB and the satellite antenna from IGS are utilized. Meanwhile, the errors like Earth rotation effect, relativity effect, phase wind-up, solid and ocean tide, phase center offset, and variation of receiver antenna are corrected by the classic models (Witchayangkoon 2000). The slant ionospheric delays and slant tropospheric delay are corrected firstly by the apriori model, then the residuals are modeled as random walk procedure and estimated. The receiver clock offset and drift as well as the receiver DCB, ISB, and IFB are also estimated as random walk parameters. The float ambiguities are estimated as random constants. The errors of position and velocity at the receiver antenna phase center are replaced by these at inertial sensor center. Then, the PSI angle error (Shin 2006) model is adopted to describe the motion status (including position and velocity) as well as the attitude at the IMU center.

For the INS data processing, besides the biases and scale factors of the gyroscopes and accelerometers being modeled as 1st Gauss–Markov procedure, the coning correction model, the rotational, and the sculling effect caused by the motion of the inertial axes are corrected to eliminate their influences on the velocity and attitude update in the INS mechanization (Farrell and Barth 1999; Shin 2006).

Finally, the GNSS/INS data will be processed in the single-GPS and multi-GNSS SF-PPP model based on: (1) single-frequency ionosphere-free combination (IF SF-PPP); (2) zenith ionospheric delay estimation (ZIDE SF-PPP); (3) slant ionospheric delay and receiver hardware time delay constraint (IC SF-PPP); (4) INS augmentation and slant ionospheric delay and receiver hardware time delay constraint (IC SF-PPP/INS). To evaluate the performance of these single-frequency PPP modes, the positioning solutions of the integration between the fixed post-positioning kinematic (the post-processing mode of the real-time kinematic) and the INS calculated by the Inertial Explorer software from NovAtel company is treated as the reference values in this paper. The trajectories calculated by these positioning modes are depicted in Fig. 2.

3.2 Satellites availability and continuity

Figures 3 and 4 demonstrate the available satellite numbers and the corresponding PDOP of the GPS, GPS + BDS (GBS), and GPS + GLONASS + BDS (GRB) along with the land-born vehicle trajectory, respectively. During the whole test, the available GPS satellite numbers are almost more than 4 excepting some few seconds, which means that this experiment is arranged in an open-sky environment. However, it is significant that the satellite availability and users–satellite geometry structure can be ameliorated visibly by using the two-constellation GNSS data (GPS + BDS) and

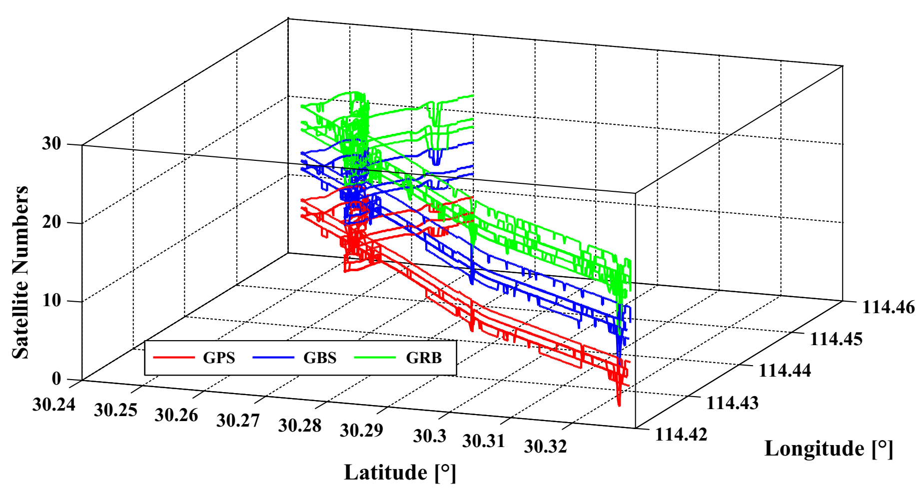

Fig. 3 Available GPS/BDS/GLONASS satellite numbers along with the vehicle trajectory; here G, B, and R refer, respectively, to GPS, BDS, and GLONASS

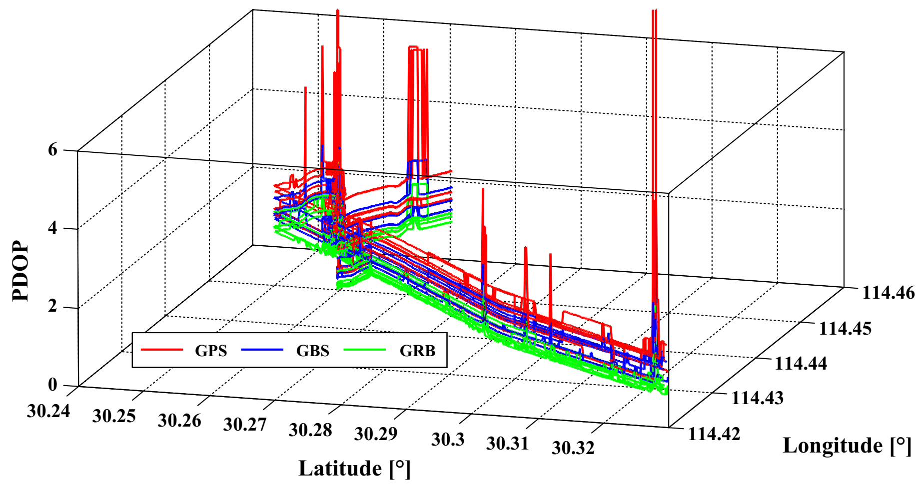

Fig. 4 PDOPs of GPS/BDS/GLONASS along with the vehicle trajectory; G, B, and R represent GPS, BDS, and GLONASS, respectively

three-constellation GNSS data (GPS + GLONASS + BDS) compared to those using the GPS only. This makes it be much more potential to achieve better positioning solutions using the SF-PPP in future dynamic applications. According to the statistics from Figs. 3 and 4, the average satellite numbers of GPS, GBS, and GRB are 8.6, 14.8, and 20.5, and the corresponding PDOP values are 2.1, 1.7, and 1.4, respectively. Significantly, the available satellite number of the multi-GNSS is about 1.5–2.5 times larger than that of the GPS only, and the improvements of PDOPs are about 19.1–33.3%. It can be concluded that there will be more available satellites and better PDOP when the GPS, BDS, GLONASS, and Galileo four-satellite systems are all available.

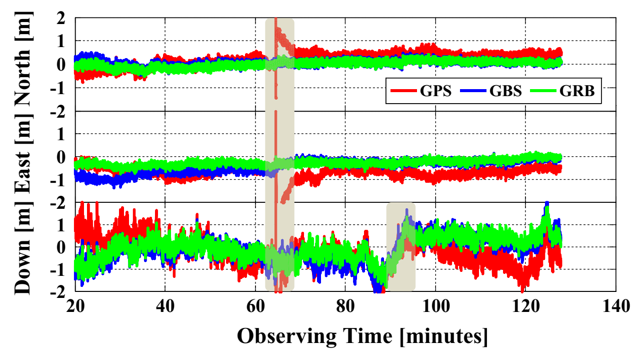

Fig. 5 Position differences of the single-frequency ionosphere-free combination PPP using the GPS, GPS + BDS (GBS), and GPS + GLONASS + BDS (GRB) observations

4 Validation and discussion

In this part, the positioning accuracy of the SF-PPP and the INS-augmented SF-PPP will be validated and evaluated in detail in both open-sky and challenged observing environmental conditions which are realized by applying the GNSS outage simulation.

4.1 Performance of different multi-GNSS SF-PPP models

The performance of the IF SF-PPP, the ZIDE SF-PPP, and the IC SF-PPP using the single-GPS, two-constellation GNSS data, and three-constellation GNSS observations are evaluated by making difference between the solutions with the reference solutions. Then, such coordinate differences are transformed from e-frame to n-frame. Table 1 shows the position differences RMS values of these three single-frequency PPP models.

According to the statistics for the position differences of the IF SF-PPP in Fig. 5, the position RMSs of the GPS + BDS + GLONASS IF SF-PPP are 16.8, 32.9, and 63.4 cm in North, East, and Down components, with 15.2, 39.9, and 15.1% enhancements and 57.8, 55.1, and 18.3% improvements compared to the GPS + BDS IF SF-PPP solutions and the single-GPS IF SF-PPP solutions as shown in Table 1.When these GNSS data are processed in the ZIDE SF-PPP model, visible improvements can be obtained by comparing the position differences time series in Fig. 6 with the values in Fig. 5, especially in the east and vertical directions. Generally, about 1.9, 17.1, and 37.3% average position enhancements in north, east, and down components can be achieved compared to the IF SF-PPP. Similarly, the multi-GNSS can also upgrade the position RMS of the ZIDE SF-PPP from 39.6, 59.3, and 66.4 cm to 16.8, 25.6, and 32.3 cm with about 55.8, 36.9, and 46.7% average improvements in north, east, and down components, respectively.

Besides the position RMS, the position instability of the IF SF-PPP is also obviously worse than that of the ZIDE SF-PPP. It is mainly due to the fact that the single-frequency ionosphere-free combination not only pollute and enlarge the observation noise of the carrier phase, but also bring the undisposed receiver hardware time delay on the pseudorange to the carrier phase, which makes the carrier-phase

Table 1 Position RMS of the single-frequency PPP using the GPS/BDS/GLONASS data based on the single-frequency ionosphere-free combination, the zenith ionospheric delays estimation, and the slant ionospheric delays and receiver DCB constraint, respectively

GNSS	IF SF-PPP			ZIDE SF-PPP			IC SF-PPP		
	North	East	Down	North	East	Down	North	East	Down
GPS (cm)	39.6	73.2	77.6	39.9	59.3	66.4	39.9	51.2	65.9
GBS (cm)	19.8	54.7	74.7	18.5	49.2	38.5	16.4	48.2	37.0
GRB (cm)	16.8	32.9	63.4	16.8	25.6	32.3	16.2	24.5	29.8

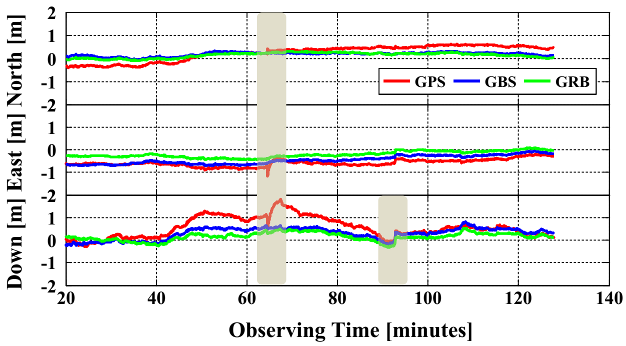

Fig. 6 Position differences of the SF-PPP based on the zenith ionospheric delays estimation model using the GPS, GPS + BDS (GBS), and GPS + GLONASS + BDS (GRB) observations

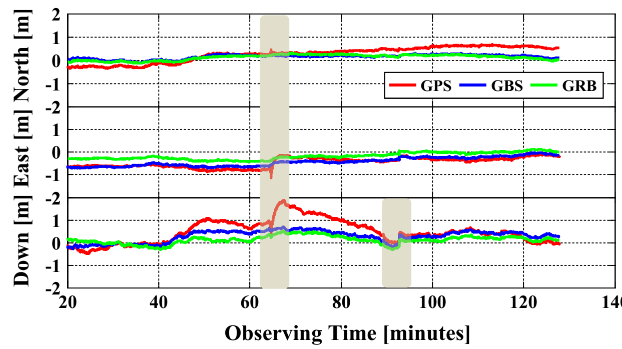

Fig. 7 Position differences of the SF-PPP based on the slant ionospheric delay and the receiver DCB constraint model using the GPS, GPS + BDS (GBS), and GPS + GLONASS + BDS (GRB) observations

quality about 100 times worse than the original one. Besides, the receiver hardware time delay will impact on ambiguity convergence. For the ZIDE SF-PPP model, the undisposed receiver hardware time delay only influences on the accuracy of the pseudo-range, and the carrier phase will keep it with high accuracy which is the key issue for precise positioning.

The influence of the receiver DCB on the ZIDE SF-PPP could be removed in the IC SF-PPP model. According to previous studies, the receiver DCB on the pseudo-range can influence the position accuracy of the PPP particularly in the convergence period (Zhang et al. 2013). Different from the ZIDE SF-PPP mode, the ionospheric delay for each satellite in the inclined signal path is estimated directly in the IC SF-PPP model. Shown in Fig. 7 is the position difference time series of the IC SF-PPP, and the corresponding position RMSs are listed in Table 1. Generally, the performance of the IC SF-PPP is significantly better than the other two SF-PPP models. The statistics indicate that the position accuracy of the IC SF-PPP can be also visibly upgraded by using the multi-GNSS data with the position RMSs of16.2, 24.5, and 29.8 cm in north-east-down directions, respectively, while using the three-constellation GNSS data. By comparing the results in Fig. 7 with those in Figs. 5 and 6, about 6.7, 22.5, and 39.5% average position improvements and about 5.0, 6.7, and 4.1% mean position enhancements in north, east, and down components can be obtained respectively.

In addition, a significant reconvergence process is emerged in the GPS IF SF-PPP (the gray area), but it is not noticeable

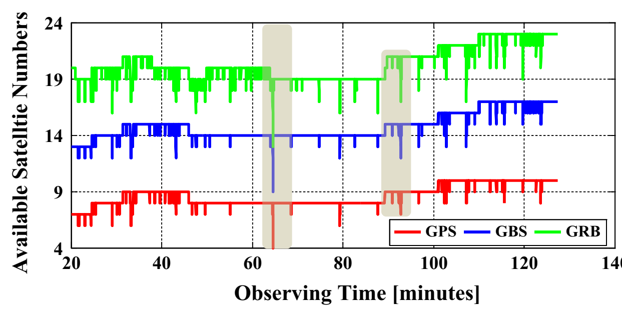

Fig. 8 Available satellite numbers of the GPS, GPS + BDS (GBS), and GPS + GLONASS + BDS (GRB) varying along with observing time

when using the multi-GNSS data and/or using the ZIDE/IC SF-PPP model, especially in the horizontal components. It is mainly due to the fact that (1) multi-GNSS systems can provide more available satellite observations than a single GPS does (seen in Fig. 8), and make the PDOP much better (Li and Shen 2009); (2) the slant ionospheric delays and receiver DCBs are rather stable in short time period (Zhang et al. 2013), which can provide strong constraints for parameter estimation in the IC SF-PPP (Gao et al. 2015). Therefore, while adopting the final GIM model provided by IGS as the ionospheric constraints, the positioning performance of the SF-PPP in terms of RMS, stability, and continuity can be ameliorated remarkably by employing the multi-GNSS data and adding the constraint models on the slant ionospheric delays and receiver DCBs. Finally, about 59.1, 66.5, and 61.6% position improvements respectively for the SF-PPP in north, east, and down components can be obtained by applying these methods together. However, according to the theoretical method of the IC SF-PPP mentioned in Sect. 2, the performance of such PPP could be partially influenced by the accuracy of the apriori ionospheric model, which means that higher accurate ionospheric models may provide a better positioning performance and lower accurate models may lead to a worse positioning solutions. From the previous studies (Hernández-Pajares et al. 2009; Zhang et al. 2013), the accuracy of the current GIM model could be up to 2 TECU. Hence, if a higher accurate ionospheric model (Shi et al. 2012; Yao et al. 2013) is provided, a much better IC SF-PPP accuracy in solutions will be obtained.

4.2 INS-augmented multi-GNSS IC SF-PPP performance

The works on the dual-frequency PPP/INS integration system have demonstrated that the performance of the dual-frequency PPP can be upgraded significantly with the aid of the INS (Roesler and Martell 2009; Rabbou and El-Rabbany 2015; Gao et al. 2015, 2016). Shown in Fig. 9 are the position differences of the IC SF-PPP/INS integration using the GPS, GPS + BDS, GPS + GLONASS + BDS, and MEMS IMU data. Compared to the solutions as shown in Fig. 7, the noticeable position improvements can be obtained,

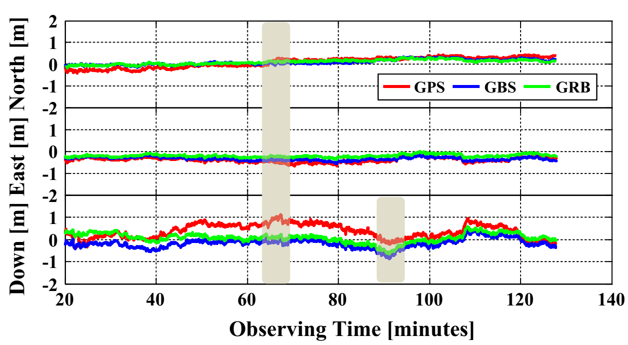

Fig. 9 Position differences of INS (MEMS IMU)-augmented SF-PPP based on the slant ionospheric delay and receiver DCB constraint model using GPS, GPS + BDS (GBS), and GPS + GLONASS + BDS (GRB) observations

especially in vertical components. According to the statistics in Table 2, the position RMSs of the INS-augmented GPS IC SF-PPP in north, east, and down components are 25.4, 40.8, and 48.3 cm, respectively, with about 26.3, 20.3, and 26.7% percentage improvements compared to the RMSs of the GPS IC SF-PPP. Analogously, visible enhancements can also be achieved while using the GPS + BDS or the GPS + GLONASS + BDS data, and the mean improvements of the position RMS for each direction are 18.3, 19.2, and 25.8%, respectively. Briefly, the final position RMSs of the SF-PPP can be improved from 39.6, 73.2, and 77.6 cm of the GPS IF SF-PPP to 14.5, 21.9, and 22.3 cm of the INS-augmented GPS + GLONASS + BDS IC SF-PPP with about 63.4, 70.1, and 71.3% percentages enhancements totally.

Besides, compared to the solutions as shown in Figs. 5, 6 and 7, we can see clearly that the position jumps caused by the insufficient satellite observations in all the three components disappeared completely as shown in Fig. 9, even only using the single GPS data. Generally, it is due to the effect of the INS that can provide users continuous navigation information with high rate and high accuracy in short time period by making digital integral on the IMU measurements (Siouris 1993; Shin 2006). Meanwhile, the parameterized IMU biases and scale factors are confirmed being stable in time domain (Gao et al. 2015). Such characters can provide external information to express a strong constraint on the parameter estimation and prevent the positioning solutions divergence of the INS-augmented IC SF-PPP. Therefore, we can obtain much better position results in dynamic applications while utilizing the augmented SF-PPP model introduced in this paper. Meanwhile, according to the SF-PPP solutions in this paper, the initial convergence of the IF SF-PPP model is worse than the other three SF-PPP models, and the difference among the initial convergence of the ZIDE SF-PPP, the IC SF-PPP, and the IC SF-PPP/INS is not noticeable. For the IF/ZIDE/IC SF-PPP modes, it due to the factor that the initial convergence of the SF-PPP is mainly determined by the qualities of the pseudo-range and the carrier phase which is similar to the positioning reasons mentioned in detail above. For the IC SF-PPP model with and without the INS augmentation, the INS-related information can only provide strong constraints to enhance the positioning performance of the IC SF-PPP after the INS-related errors are estimated accurately or the errors of the IMU are very small. But the MEMS IMU's

Table 2 Position RMS of the INS-augmented IC SF-PPP and the corresponding position improvement percentages by comparing the INS-augmented IC SF-PPP with the IC SF-PPP

GNSS	Position RMS (cm)			Attitude RMS (°)			Position improvements (%)		
	North	East	Down	Roll	Pitch	Heading	North	East	Down
GPS	25.4	40.8	48.3	0.342	0.099	0.571	36.3	20.3	26.7
GBS	15.8	35.4	27.6	0.341	0.099	0.570	7.9	26.6	25.4
GRB	14.5	21.9	22.3	0.339	0.099	0.558	10.5	10.6	25.2

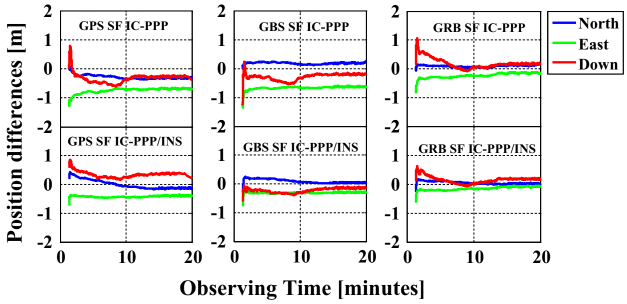

Fig. 10 Initial positioning performance of the IC SF-PPP model with and without the INS augmentation using GPS, GPS + BDS (GBS), and GPS + GLONASS + BDS (GRB) observations

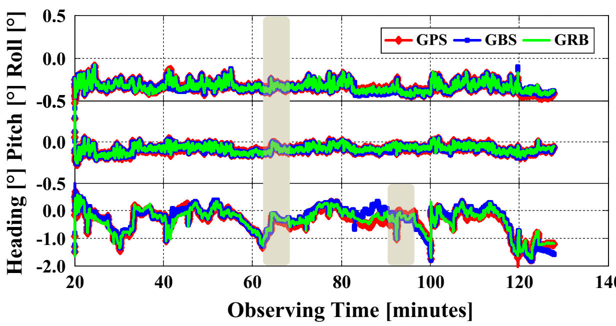

Fig. 11 Attitude differences of the INS (MEMS IMU)-augmented SF-PPP based on the slant ionospheric delay and the receiver DCB constraint model using the GPS, GPS + BDS (GBS), and GPS + GLONASS + BDS (GRB) observations

errors are big and the INS-related parameters cannot be estimated precisely in a short time period in the IC SF-PPP/INS model, which leads to its initial convergence being improved indistinctively. As is shown in Fig. 10, the convergence performance of both SF-PPP mode and SF-PPP/INS integration mode are mainly depended on multi-GNSS systems, the more GNSS systems applied the better convergence performance can be obtained. The influence of INS in this test seems to make the solutions stable and smooth. The reason may be that the observation numbers of the SF IC-PPP mode (3*n) are much less than that in the DF IC-PPP mode (5*n), which degrades the effect of INS in improving SF PPP convergence performance. However, it is proved that the initial convergence of dual-frequency PPP can be improved visibly by the augmentation of the INS (Gao et al. 2016). Besides, theoretically, the initial convergence of the SF-PPP can be speeded up when using the high grade IMU sensors (e.g., the tactical grade, the navigation grade).

Besides the positioning solutions, the INS-augmented IC SF-PPP can also provide attitudes in terms of Roll, Pitch, and Heading. Plotted in Fig. 11 are the attitude time series by making difference between the attitude solutions of the INS-augmented IC SF-PPP and the reference values. According to the corresponding RMSs listed in Table 2, the average RMSs of Roll, Pitch, and Heading are 0.341°, 0.099°, and 0.566°, respectively. The attitude RMS differences among the INS-augmented IC SF-PPP using different GNSS observations are almost within ±0.01°. Similar results can also be found from the study on the INS-augmented dual-frequency multi-GNSS PPP of Gao et al. (2016). Theoretically, in the GNSS/INS integration system, attitudes will become observable by the positioning update when the vehicle makes maneuvers (e.g., steering or accelerating). In this case, the changes of the positioning information will slightly affect the attitude estimation. Besides, the estimation accuracy of attitude also can be affected slightly by other parameters' estimation in the Kalman filtering, therefore the GNSS/INS integration system based on different positioning techniques and different GNSS observations will provide the attitude solutions with little differences in accuracy. Shown in Fig. 12 are the estimated biases of the IMU sensors in *b*-frame. In general, the IMU biases vary slowly along with the IMU operating time. Clearly, there are small differences among the IMU biases estimated in the INS-augmented IC SF-PPP using different GNSS data. Such differences are within ±0.17 cm/s^2 and 0.09°/h for accelerometers and gyroscopes respectively according to the statistics.

4.3 Performance of INS-augmented IC SF-PPP in challenge conditions

For the most of the land-borne dynamic applications, it is common to pass the big buildings, overpasses, shades, and tunnels, etc., especially in city canyon. In these conditions, both the single-GPS and multi-GNSS may partially or completely lose the satellite signals tracking. The frequent GNSS signal loss will destroy the continuity of the GNSS observation leading to the frequent reconvergence processing in the PPP calculation and evidently degrading the PPP accuracy. It is one of the main factors limiting the application of the PPP in dynamic domain for both of the DF-PPP and SF-PPP. To analyze the performance of the INS-augmented IC SF-PPP in these conditions, beginning from 23.3 min, seven GNSS outage scenes (each scene lasts for 30 s with 1000 s available GNSS data following) are added to the observed GNSS data with simulating unavailable satellites in each GNSS outage scenes. Then, the whole data are processed in the IC SF-PPP and the INS-augmented IC SF-PPP using the GPS, GPS + BDS, and GPS + GLONASS + BDS, respectively. Depicted in Figs. 13 and 14 are the time series of the velocity and the attitude which show the dynamics of the vehicle during each simulated GNSS outage directly. The black regions (s1, s2, s3… s7) represent the simulated GNSS outage periods. When the s3, s5, and s7 happened, there were little changes of the vehicle motion state and they almost kept the linear motion, which can be seen clearly from the changes of the horizontal velocity and the heading angle during these

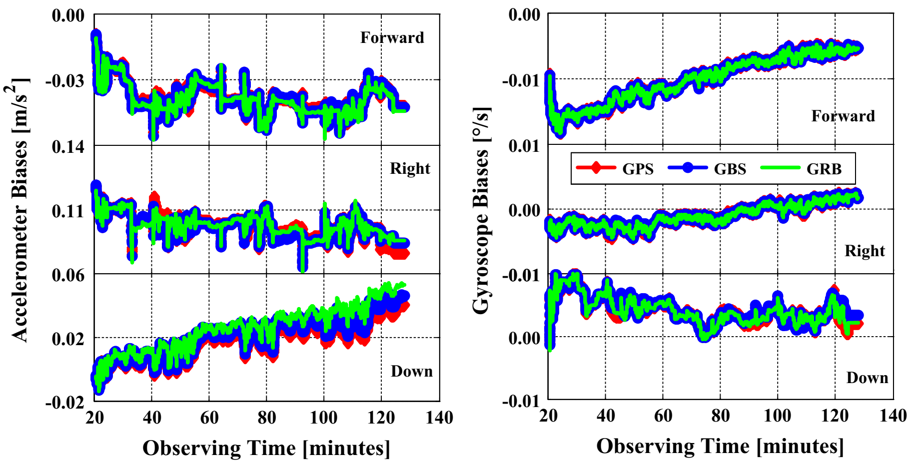

Fig. 12 In body frame (Forward-Right-Down), the biases and scale factors of accelerometer (*left*) and gyroscope *right*) estimated by the INS-augmented IC SF-PPP using the GPS, GPS + BDS (GBS), and GPS + GLONASS + BDS (GRB)

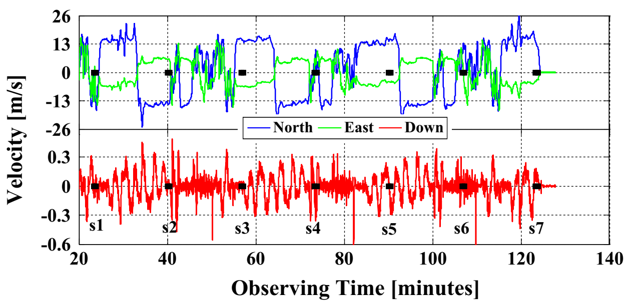

Fig. 13 Velocity time series of the vehicle during the whole test; s1, s2, s3…s7 denote the simulated GNSS outage periods

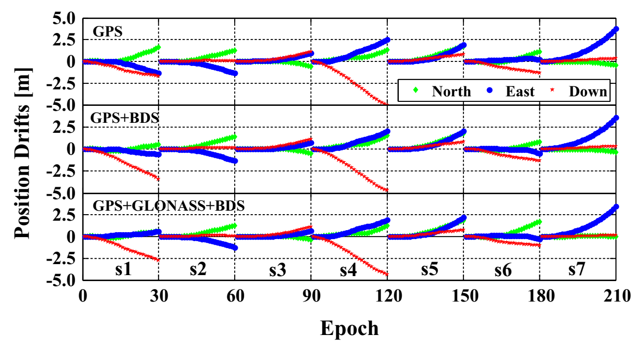

Fig. 15 Position drifts of the INS-augmented IC SF-PPP during the GNSS outage periods (s1–s7 are GNSS outage simulations) using the GPS, GPS + BDS, and GPS + GLONASS + BDS data

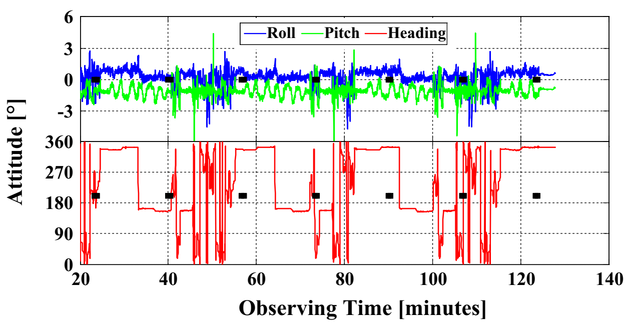

Fig. 14 Attitude time series of the vehicle during the whole test; s1, s2, s3…s7 denote the simulated GNSS outage periods

periods. Similarly, we can also conclude that for the other GNSS outage periods, the dynamics of vehicle is not linear and is complex.

4.3.1 *Performance of MEMS INS during GNSS outage periods*

During the partial and complete GNSS outage periods, the IC SF-PPP cannot work anymore, but the INS-augmented IC SF-PPP can still work in the INS-augmented mode and the INS mechanization mode. However, the accuracy of these results will degrade along with the increasing GNSS outage time. In the complete GNSS outage situations, the position drifts calculated by the INS mechanization using the MEMS IMU data are plotted in Fig. 15, and the corresponding position drifts RMS and the maximum values along with the GNSS outage time are listed in Table 3. Significantly, the position RMSs in north, east, vertical components degrade dramatically from 1.2, 0.6, and 2.7 cm to 119.9, 193.7, and 221.2 cm along with the GNSS outage time increasing from 1 s to 30 s, and the maximum drifts are even up to 185.5, 378.7, and 502.4 cm. It is mainly due to the time varying character of the IMU errors (as shown in Fig. 12) during the GNSS outage. These errors estimated before the GNSS outage occurring can only be utilized to remove the collective errors, but the extra increments of the IMU errors cannot be estimated or compensated because of lack of external observations. Then, these undisposed IMU errors will lead the position solutions from the INS to deviate rapidly. Generally, when the GNSS outage time is no more than about 15 s, a sub-meter position RMS can be obtained. Theoretically, the position accuracy during the GNSS outage time is determined only by INS, hence the solutions of the INS-aided IC

Table 3 RMS and maximum of position drifts of the INS-augmented IC SF-PPP for the different GNSS outage timescales

Items	Time	1 s	5 s	10 s	15 s	20 s	25 s	30 s
RMS (cm)	North	1.2	4.9	15.2	27.5	52.1	86.4	119.9
	East	0.6	5.3	19.6	46.6	86.2	138.0	193.7
	Down	2.7	20.8	55.8	100.7	146.4	190.5	221.2
MAX (cm)	North	3.3	9.4	30.2	49.1	95.7	145.3	185.5
	East	0.9	13.2	46.2	95.5	167.8	269.8	378.7
	Down	6.4	49.4	128.8	226.1	334.1	438.6	502.4

SF-PPP using different GNSS data present slight difference to each other. Clearly, it is owning to the different estimation accuracy of the IMU sensors' biases and scale factors. Because, before the increments of the velocity and angle can be utilized in the INS mechanization, all of them should be compensated firstly to remove the impacts of the biases and scale factors on the performance of the INS as much as possible. Hence, when the IMU data are compensated by different accuracy biases and scale factors (as shown in Fig. 12), it will inevitably result in solutions with little different accuracies.

4.3.2 *INS-augmented IC SF-PPP working in frequent GNSS outage environments*

After each GNSS outage, when there are available GNSS data, the INS-augmented IC SF-PPP works well. If the available satellite number reaches the minimum required in the IC SF-PPP, it still works. Figures 16 and 17 plot the position differences of the IC SF-PPP without and with the INS augmentation, respectively, and the corresponding RMSs are listed in Table 4. Comparing the results shown in Fig. 16 with those shown in Fig. 17, we can see obviously that (1) the solutions of the IC SF-PPP with the INS augmentation are much better than those of the IC SF-PPP; (2) the multi-GNSS data can improve the solutions of the two positioning modes.

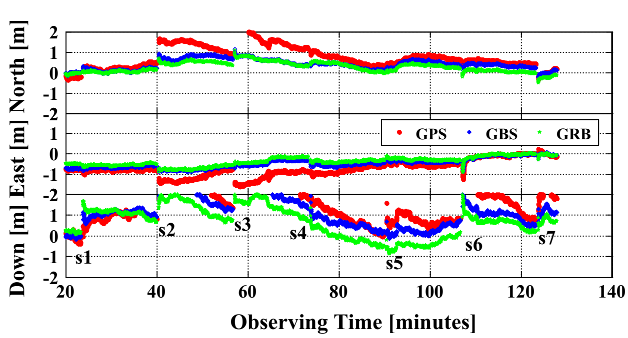

Fig. 16 In the GNSS outage simulations, the position differences of the IC SF-PPP using the GPS, GPS + BDS (GBS), and GPS + GLONASS + BDS (GRB) observations; s1–s7 indicate the GNSS outage simulations

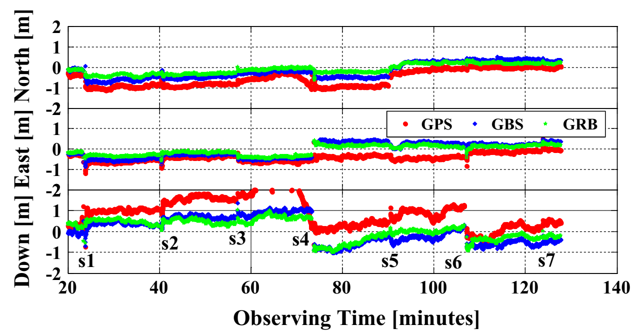

Fig. 17 In the GNSS outage simulations, the position differences of the INS-augmented IC SF-PPP using the GPS, GPS + BDS (GBS), and GPS + GLONASS + BDS (GRB) observations; s1–s7 indicate the GNSS outage simulations

Table 4 In the GNSS outage simulations, the position RMS of the IC SF-PPP using the GPS, GPS + BDS (GBS), and GPS + GLONASS + BDS (GRB) observations, respectively

GNSS	IC SF-PPP			IC SF-PPP/INS		
	North	East	Down	North	East	Down
GPS (cm)	93.5	83.1	206.9	67.5	45.4	112.5
GBS (cm)	46.9	53.1	132.3	42.7	37.5	61.4
GRB (cm)	35.8	43.6	98.9	25.8	24.3	47.8

Accordingly, the position RMSs in north, east, and down directions are enhanced visibly from 93.5, 83.1, and 206.9 cm of the GPS IC SF-PPP to 35.8, 43.6, and 98.9 cm of the GPS + BDS + GLONASS IC SF-PPP with 61.7, 47.5, and 52.2% improvements, respectively. Statistically, about 55.8, 41.8, and 44.1% enhancements can be achieved when the GPS + BDS data and the GPS + BDS + GLONASS data are utilized in the IC SF-PPP. In the INS-augmented IC SF-PPP mode, similar conclusions can also be obtained while comparing the position solutions from single GPS with those from multi-GNSS. Finally, about 25.8, 24.3, and 47.8 cm position RMSs can be obtained while applying the multi-GNSS data and the MEMS inertial measurements to the IC SF-PPP together, and about 21–50% position improvements can be obtained. Besides, comparing the position RMSs of the IC SF-PPP with those of the INS-augmented IC SF-PPP, the average position improvements are 21.6, 39,7, and 50.3% in the three components. Meanwhile, from Figs. 16 and 17, we can also see that faster reconvergence process of the SF-PPP can be achieved by applying both the multi-GNSS data and the INS data.

5 Conclusions

A multi-GNSS SF-PPP model augmented by the slant ionospheric delays and receiver DCB constraint model and the inertial measurements is presented in detail in this contribution, and the corresponding software is also designed and implemented. Then, the algorithm is evaluated and validated by analyzing a set of land-borne vehicle experiment data.

According to the results, we conclude that (1) multi-GNSS observations can improve the performance of the SF-PPP significantly; (2) the position performance of the SF-PPP in terms of the position RMS and continuity can be upgraded significantly by using the slant ionospheric delay and receiver DCB-constrained SF-PPP model; (3) with the augmentation of the INS, the performance of the slant ionospheric delay and the receiver DCB-constrained multi-GNSS SF-PPP can be further improved to 14.5, 21.9, and 22.3 cm with about 10.5, 10.6, and 21.9% percentages enhancements in north, east, and vertical components, respectively. Besides the high accuracy in positions, acceptable attitudes can also be obtained in this model. In addition, the results from the GNSS outage simulations indicate that the performance of the SF-PPP in terms of the position RMS, continuity, and reconvergence time can be refined significantly with the help of the multi-GNSS and the INS, except that the positioning accuracy of the INS degrades dramatically along with the increasing GNSS outage time.

With rapid development of the multi-constellation GNSS systems, much more navigation satellites can be observed at every epoch, which will provide the single-frequency users better continuous observations and higher positioning accuracy, especially after all of the four-satellite navigation systems being of global coverage. Besides, along with development of the low-cost IMU production technology, more and more cheaper and better performance MEMS IMU will be produced, and the INS-augmented SF-PPP model investigated here makes the performance of the SF-PPP in both the open-sky conditions and challenged environments much better compared to the current SF-PPP models, which makes it potential in consumer applications.

Acknowledgements This work was supported partly by National 973 Project of China (Grant Nos. 2013CB733301 and 2013CB733305), National Natural Science Foundation of China (Grant Nos. 41128003, 41210006, 41429401, 41574007), DAAD (Grant No. 57173947), NASG Special Project Public Interest (Grant No. 201512001) and the national key research and development program of China (Grant No. 2016YFB0501804).

References

Azúa BM, DeMets C, Masterlark T (2002) Strong interseismic coupling, fault after slip, and viscoelastic flow before and after the Oct. 9, 1995 Colimac Jalisco earthquake: continuous GPS measurements from Colima, Mexico. Geophys Res Lett 29(8):122

Beran T, Kim D, Langley RB (2003) High-precision single-frequency GPS point positioning. In: Proceedings of the 16th international technical meeting of the satellite division of the institute of navigation, Portland, OR, USA, p 912

Beran T, Bisnath SB, Langley RB (2004) Evaluation of high-precision, single-frequency GPS point positioning models. In: ION GNSS, pp 1893–1901 (2004)

Bisnath S, Gao Y (2009) Current state of precise point positioning and future prospects and limitations. In: Observing our changing earth. Springer, Berlin, pp 615–623

Bock H, Hugentobler U, Beutler G (2003) Kinematic and dynamic determination of trajectories for low Earth satellites using GPS. In: First CHAMP mission results for gravity, magnetic and atmospheric studies. Springer, Berlin, pp 65–69

Böhm J, Niell A, Tregoning P, Schuh H (2006) Global mapping function (GMF): a new empirical mapping function based on numerical weather model data. Geophys Res Lett 33:L7304. doi:10.1029/2005GL025546

Brown RG, Hwang PYC (1992) Introduction to random signals and applied Kalman filtering. Willey, New York

Cai C, Liu Z, Luo X (2013) Single-frequency ionosphere-free precise point positioning using combined GPS and GLONASS observations. J Navig 66(03):417–434

Cox DB (1978) Integration of GPS with inertial navigation systems. Navigation 25(2):236–245

Crespillo OG, Heirich O, Lehner A (2014) Bayesian GNSS/IMU tight integration for precise railway navigation on track map. In: 2014 IEEE/ION position, location and navigation symposium-PLANS, pp 999–1007 (2014)

Du S (2010) Integration of precise point positioning and low cost MEMS IMU. Unpublished masters dissertation, University of Calgary, Calgary, Canada

Dach R, Hugentobler U, Fridez P, Meindl M (2007) Bernese GPS software version 5.0. Astronomical Institute, University of Bern, 640, 114

Farrell JA, Barth M (1999) The global positioning systems and inertial navigation. McGraw-Hill, New York

Gao Y, Shen X (2002) A new method for carrier-phase-based precise point positioning. Navigation 49(2):109–116

Gao Y, Zhang Y, Chen K (2006) Development of a real-time single-frequency precise point positioning system and test results. In: Proceedings of ION GNSS, pp 26–29

Gao Z, Zhang H, Ge M, Niu X, Shen W, Wickert J, Schuh H (2015) Tightly coupled integration of ionosphere-constrained precise point positioning and inertial navigation systems. Sensors 15(3):5783–5802

Gao Z, Shen W, Zhang H, Niu X, Ge M (2016) Real-time kinematic positioning of INS tightly aided multi-GNSS ionospheric constrained PPP. Sci Rep 6:30488. doi:10.1038/srep30488

Ge M, Gendt G, Rothacher MA, Shi C, Liu J (2008) Resolution of GPS carrier phase ambiguities in precise point positioning (PPP) with daily observations. J Geod 82(7):389–399

Gendt G, Dick G, Reigber CH, Tomassini M, Liu Y, Ramatschi M (2003) Demonstration of NRT GPS water vapor monitoring for numerical

weather prediction in Germany. J Meteorol Soc Jpn 82(1B):360–370
Geng J, Meng X, Dodson AH, Ge M, Teferle FN (2010) Rapid re-convergences to ambiguity-fixed solutions in precise point positioning. J Geod 84(12):705–714
Geng J, Teferle FN, Meng X, Dodson AH (2011) Towards PPP–RTK: ambiguity resolution in real-time precise point positioning. Adv Space Res 47(10):1664–1673
Grejner-Brzezinska DA, Da R, Toth C (1998) GPS error modeling and OTF ambiguity resolution for high-accuracy GPS/INS integrated system. J Geod 72(11):626–638
Hernández-Pajares M, Juan JM, Sanz J, Orus R, Garcia-Rigo A, Feltens J, Krankowski A (2009) The IGS VTEC maps: a reliable source of ionospheric information since 1998. J Geod 83(3–4):263–275
Héroux P, Gao Y, Kouba J, Lahaye F, Mireault Y, Collins P, Chen K (2004) Products and applications for precise point positioning-moving towards real-time. In: Proceedings of the 17th international technical meeting of the satellite division of The Institute of Navigation (ION GNSS 2004), pp 1832–1843
Héroux P, Kouba J (1995) GPS precise point positioning with a difference. Natural Resources Canada, Geomatics Canada, Geodetic Survey Division
Kim J, Jee GI, Lee JG (1998) A complete GPS/INS integration technique using GPS carrier phase measurements. In: Position location and navigation symposium, IEEE, pp 526–533 (1998)
Kleusberg A, Teunissen PJG (1996) GPS for geodesy. Lecture notes in earth sciences. Springer, Berlin, p 60
Kouba J (2013) A guide to using international GNSS service (IGS) products. In: Ocean Surface Topography Science Team (OSTST) Meeting in Boulder, CO
Larson KM, Bodin P, Gomberg J (2003) Using 1-Hz GPS data to measure deformations caused by the Denali fault earthquake. Science 300(5624):1421–1424
Le AQ, Tiberius CCJM, Van der Marel H, Jakowski N (2009) Use of global and regional ionosphere maps for single-frequency precise point positioning. In: Observing our changing earth. Springer, Berlin, pp 759–769
Li B, Shen Y (2009) Global navigation satellite system ambiguity resolution with constraints from normal equations. J Surv Eng 136(2):63–71
Li X, Ge M, Zhang H, Wickert J (2013) A method for improving uncalibrated phase delay estimation and ambiguity-fixing in real-time precise point positioning. J Geod 87(5):405–416
Li X, Ge M, Dai X, Ren X, Fritsche M, Wickert J, Schuh H (2015) Accuracy and reliability of multi-GNSS real-time precise positioning: GPS, GLONASS, BeiDou, and Galileo. J Geod 89(6):607–635
Lou Y, Zheng F, Gu S, Wang C, Guo H, Feng Y (2015) Multi-GNSS precise point positioning with raw single-frequency and dual-frequency measurement models. GPS Solut. doi:10.1007/s10291-015-0495-8
Montenbruck O (2003) Kinematic GPS positioning of LEO satellites using ionosphere-free single frequency measurements. Aerosp Sci Technol 7(5):396–405
Montenbruck O, Steigenberger P, Khachikyan R, Weber G, Langley R, Mervart L, Hugentobler U (2014) IGS-MGEX: preparing the ground for multi-constellation GNSS science. Inside GNSS 9(1):42–49
Niu X, Goodall C, Nassar S, El-Sheimy N (2006) An efficient method for evaluating the performance of MEMS IMUs. In: Position location and navigation symposium, 2006 IEEE/ION. San Diego, CA, USA, pp 766–771
Odijk D, Teunissen PJ, Zhang B (2012) Single-frequency integer ambiguity resolution enabled GPS precise point positioning. J Surv Eng 138(4):193–202
Øvstedal O (2002) Absolute positioning with single-frequency GPS receivers. GPS Solut 5(4):33–44
Petovello MG (2004) Real-time integration of a tactical-grade IMU and GPS for high-accuracy positioning and navigation. National Library of Canada, Ottawa
Rabbou MA, El-Rabbany A (2015) Tightly coupled integration of GPS precise point positioning and MEMS-based inertial systems. GPS Solut 19(4):601–609
Roesler G, Martell H (2009) Tightly coupled processing of precise point position (PPP) and INS data. In: Proceedings of ION GPS/GNSS, Institute of Navigation, Savannah, GA, USA, pp 1898–1905
Schaer S, Gurtner W, Feltens J (1998) IONEX: the ionosphere map exchange format version 1. In: Proceedings of the IGS AC workshop, vol 9, no 11, Darmstadt, Germany
Shi C, Gu S, Lou Y, Ge M (2012) An improved approach to model ionospheric delays for single-frequency precise point positioning. Adv Space Res 49(12):1698–1708
Shin EH, El-Sheimy N (2003) Accuracy improvement of low cost INS/GPS for land applications. National Library of Canada, Ottawa
Shin EH (2006) Estimation techniques for low-cost inertial navigation. Library and Archives Canada, Ottawa
Siouris GM (1993) Aerospace avionics systems: a modern synthesis. Academic Press, New York
Steigenberger P, Rothacher M, Fritsche M, Rülke A, Dietrich R (2009) Quality of reprocessed GPS satellite orbits. J Geod 83(3–4):241–248
Teunissen PJG, Khodabandeh A (2015) Review and principles of PPP–RTK methods. J Geod 89(3):217–240
Tu R, Ge M, Zhang H, Huang G (2013a) The realization and convergence analysis of combined PPP based on raw observation. Adv Space Res 52(1):211–221
Tu R, Zhang H, Ge M, Huang G (2013b) A real-time ionospheric model based on GNSS precise point positioning. Adv Space Res 52(6):1125–1134
Witchayangkoon B (2000) Elements of GPS precise point positioning. Doctoral dissertation. University of New Brunswick
Xu P, Shi C, Fang R, Liu J, Niu X, Zhang Q, Yanagidani T (2013) High-rate precise point positioning (PPP) to measure seismic wave motions: an experimental comparison of GPS PPP with inertial measurement units. J Geod 87(4):361–372
Yang Y, Li J, Xu J, Tang J, Guo H, He H (2011) Contribution of the compass satellite navigation system to global PNT users. Chin Sci Bull 56(26):2813–2819
Yunck TP (1996) Orbit determination. In: Parkinson BW, Spilker JJ (eds) Global positioning system-theory and applications. AIAA, Washington
Yao Y, Zhang R, Song W, Shi C, Lou Y (2013) An improved approach to model regional ionosphere and accelerate convergence for precise point positioning. Adv Space Res 52(8):1406–1415
Zhang Y, Gao Y (2005) Performance analysis of a tightly coupled Kalman filter for the integration of un-differenced GPS and inertial data. In: Proceedings of the 2005 national technical meeting of The Institute of Navigation, pp 270–275
Zhang X, Li X (2012) Instantaneous re-initialization in real-time kinematic PPP with cycle slip fixing. GPS Solut 16(3):315–327
Zhang H, Gao Z, Ge M, Niu X, Huang L, Tu R, Li X (2013) On the convergence of ionospheric constrained precise point positioning (IC-PPP) based on undifferential uncombined raw GNSS observations. Sensors 13(11):15708–15725
Zumberge JF, Heflin MB, Jefferson DC, Watkins MM, Webb FH (1997) Precise point positioning for the efficient and robust analysis of GPS data from large networks. J Geophys Res Solid Earth 102(B3):5005–5017